Experimental determination of bearing performance of the VentrAssist rotary blood pump

Chung M [a], Zhang N [a], Tansley GD [b] and Woodard JC [b]

[a] *Faculty of Engineering, University of Technology, Sydney, 1 Broadway NSW 2007, Australia*

[b] *VentrAssist P/L, 126 Greville Street Chatswood NSW 2067, Australia*

The VentrAssist implantable rotary blood pump, intended for long term ventricular assist, is under development and is currently being tested for its rotor-dynamic stability. The pump consists of a shaftless impeller, which also acts as the rotor of the brushless DC motor. The impeller remains passively suspended in the pump cavity by hydrodynamic forces, which result from the small clearances between the outside surfaces of the impeller and the pump cavity. These small clearances range from approximately 50 μm to 230 μm in size.

This paper presents experimental investigation of the displacement of the impeller within the cavity. Displacement of the impeller was measured using eddy-current proximity sensors and laser displacement proximity sensors, located at different positions on the pump, under different pump-operating conditions. All transducers have been calibrated prior to any experimental. Voltage output from the transducers were converted into impeller movement in five independant physical coordinates (x, y, z, θ_x and θ_y). The sixth degree of freedom (θ_z), the rotation about the impeller axis, is determined by the commutation performed by the motor controller.

To determine experimentally the dynamic characteristics of the hydrodynamic bearing, a computer program was developed to calculate the axial bearing force exerted on an impeller blade. By combining the calculated force with the measured impeller displacement, the stiffness and damping coefficients were determined.

Keywords: Rotor dynamics, hydordynamic bearing, rotary blood pump.

1. Introduction

The VentrAssist implantable rotary blood pump is based on a centrifugal design and is intended for long term ventricular assist. Currently, it is under development and being tested for its rotor-dynamic stability. It is a novel device consisting of only one moving part – a shaftless impeller. The impeller blades are imbedded with permanent magnets to enable it to act as a rotor for the pump's brushless DC motor. Due to the absence of a shaft, contact bearings and seals, the design of the pump is ideal in reducing blood trauma. Contact points between the shaft and bearings can cause damage to red blood cells, through shearing and heat, which will lead to heamolysis. Blood clots or thrombosis can also be experienced due to stagnant flow at these contact points and at the seals. Suspension of the impeller within the pump cavity is performed passively and is achieved through the use of hydrodynamic forces. Hydrodynamic suspension systems have been investigated by other parties [1,2], while others incorporate hydrodynamic bearings working in synergy with magnetic bearings for suspension [3]. Total active suspension systems are currently being utilised by other rotary blood pumps [4,5,6]; however, these incorporate more complex and larger monitoring and electrical systems. With the VentrAssist pump, monitoring sensors are eliminated due to the use of hydrodynamic bearings for passive suspension, thus requiring less complicated electronics. This results in a smaller, more electrically efficient and reliable pump requiring less electrically dependent components.

Due to the absence of monitoring sensors, shaft and contact bearings in the VentrAssist pump, the movement of the impeller within the pump cavity was unknown. Furthermore the dynamic analysis of the hydrodynamic bearing was challenging. Therefore, in this paper, the impeller displacement, during different operating conditions was evaluated experimentally through displacement measurements using eddy current proximity sensors and laser proximity sensors. Eddy current proximity sensors have been implemented in other rotary blood pumps, which incorporate magnetic

suspension [7,8]; thus the ability for these sensors to detect impeller movement is evident. The displacement corresponding to the five independent physical coordinates (x, y, z, θ_x and θ_y) about the centre of the bottom surface of the impeller was determined from the sensor measurements, while the sixth degree of freedom - θ_z; describes the rotation of the impeller and was determined by the commutation performed by the motor controller.

2. Hydrodynamic Analysis

The suspension of the impeller within the pump cavity is due to the hydrodynamic forces from the bearing [9,10], which are a result of the small clearances between the outer surfaces of the impeller and the pump cavity. These clearances range from approximately 50 μm to 230 μm in size. The properties of blood dictate the size of these clearances. One of the main concerns of blood trauma is heamolysis (destruction of red blood cells). The maximum diameter of a red blood cell is 8 μm, thus the clearances between the impeller and pump cavity are sufficient for the blood cells to travel through without being damaged. Also, these clearances will reduce the risk of red blood cell exclusion. The impeller blade surfaces incorporate a wedge design where the leading edge clearance is larger than the trailing edge clearance (50 μm difference) as shown in figure 1.

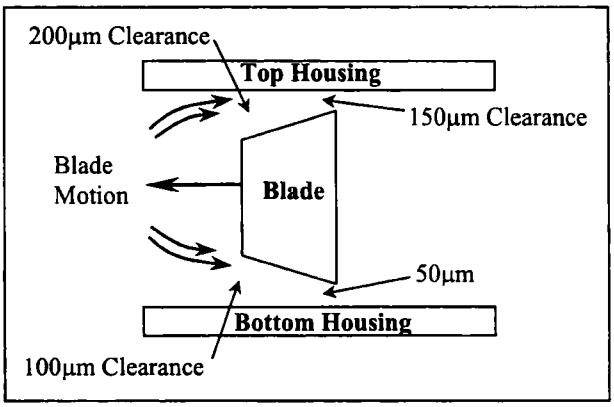

Figure 1. Example of a hydrodynamic bearing

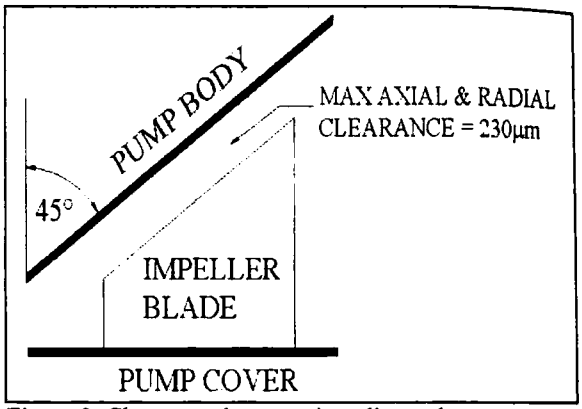

Figure 2. Clearances between impeller and pump casing

By using this wedge design, basic 2-dimensional hydrodynamic lubrication theory [11] can be applied to determine the pressure force. As the bearing clearance decreases, the pressure force increases.

With the wedge design incorporated into the VentrAssist impeller at both the top and bottom surfaces, pressure forces will exist at both these locations. In theory, an equilibrium position will be achieved when both top and bottom forces are of equal magnitude and opposite direction.

3. Materials and Method

A laboratory version of a VentrAssist C-B series pump was used for the experiment. The pump housing was made of transparent acrylic, which allowed the laser sensors to detect the displacement of the impeller. A 2.8 series impeller (figure 5) was used for the experiment and was made of titanium aluminium vanadium (Ti-6Al-4V), a biocompatible alloy. Pump and impeller descriptions are as follows: -

Cover
- Diameter of bearing pad = 40mm
- Diameter of outlet = 10mm

Body
- Diameter of inlet = 10mm
- Diameter of cone surface = 40mm
- Cone angle = 45°

Impeller

- Outside diameter = 40mm
- Inside diameter = 15.5mm
- Bottom blade surface taper height = 0.05mm
- Top blade surface taper height = 0.05mm (vertical)
- Top blade surface angle = 45°
- Mass = 35.22 g

Four eddy current proximity sensors (VK-202A – Shinkawa Electric Co., Ltd, Japan) were distributed around the pump cover at a pitch circle diameter of 30mm – two on the x-z plane and two on the y-z plane – while the two laser proximity sensors (D85386 – MEL - Eching, Germany) were located on the side of the pump (also on the x-z and y-z planes) (figure 3). Previous investigations were performed to prove the accuracy of these eddy current proximity sensors. Generally the pump will operate using six electromagnetic motor coils, three on the body and three on the cover. However, due to the interference from the actuation of the coils affecting the eddy current proximity sensors, the coils on the cover were removed to accommodate the sensors and to eliminate any interference. The electrical design of the pump allowed it to continue operating normally with only one set of coils. Hydrodynamic stability of the impeller was not jeopardised because the coils were used solely for the purpose of rotating the impeller, rather than impeller suspension. The eddy current proximity sensors were used to measure the axial (z) and angular (θx and θy) displacement of the impeller, at 90° degree (blade pass) intervals, during pump operation. While the two laser sensors located on the side were used to measure the translation of the impeller in the x and y direction.

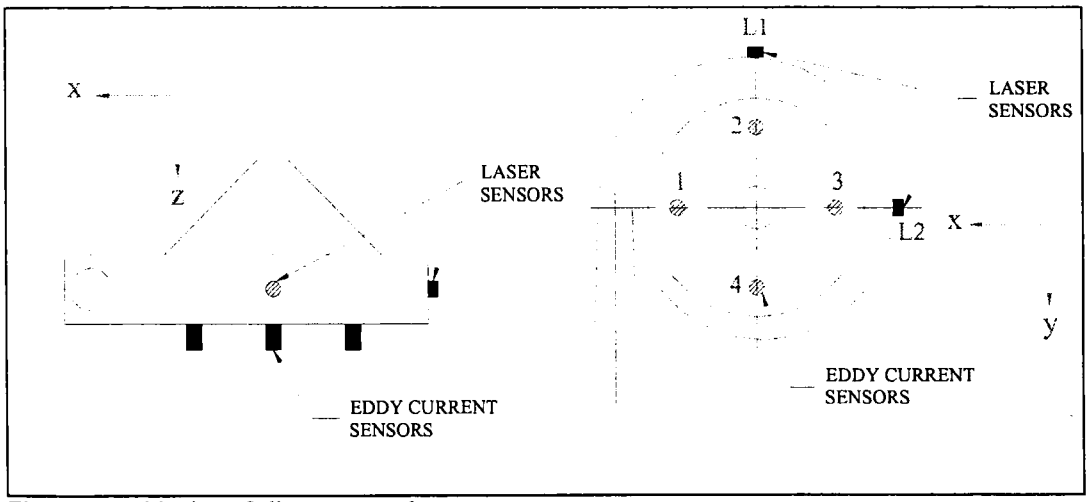

Figure 3. Positioning of all sensors on the pump

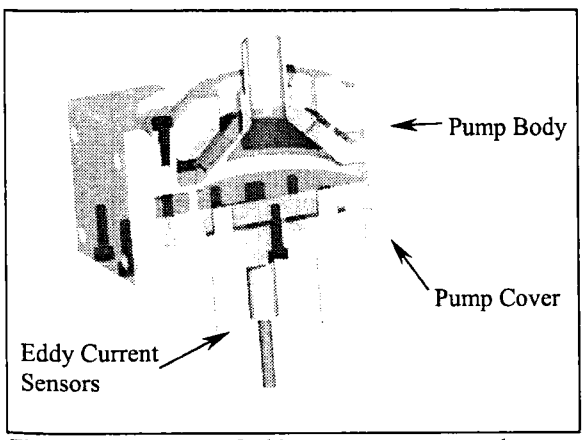

Figure 4. Placement of eddy current sensors on the pump

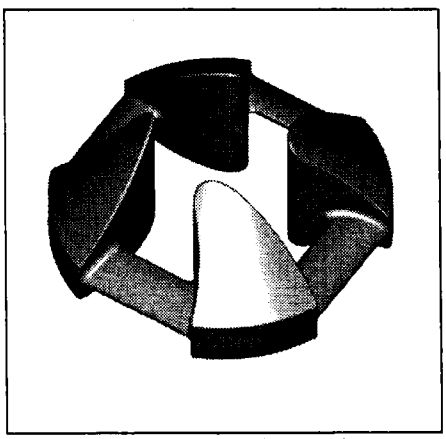
Figure 5. 2.8 series impeller used

Signal conditioners for the eddy current proximity sensors (VK-202A2 & VK-202A1, Shinkawa Electric Co., Ltd, Japan) and the laser proximity sensors (M25L/2-10B24NK – MEL – Eching, Germany) were used to condition the voltage signals from the sensors. The voltage signals were sent to an analog breakout accessory rack (BNC 2090 - National Instruments U.S.A.) and a data acquisition board (PC-LPM-16 – National Instruments U.S.A.) where the signal was displayed on a computer monitor through a data analysis software - VirtualBench™ V2.1.1 (National Instruments, U.S.A). The raw data was collected by the data acquisition software LabView™ V5.0 (National Instruments, USA).

All six sensors performed measurements simultaneously so that when a blade passed the sensors, all five displacements corresponding to the independent physical coordinates of the impeller were calculated from the output readings.

Four pump operating conditions were investigated. The speed of the pump was adjusted through the motor controller, while the flow rate was monitored by a flow probe (#10C277 – Transonic) and a flow meter (T206 - Transonic). These operating conditions were as follows: -

1. 2400 rev/min @ 3 l/min
2. 2400 rev/min @ 4 l/min
3. 2400 rev/min @ 5 l/min
4. 2400 rev/min @ 6 l/min

The pumping medium used for the experiment was 30% aqueous glycerol. Properties of 30% aqueous glycerol and blood are as follows: -

Table 1
Properties of 30% aqueous glycerol and 40% hematocrit blood

Property	Aqueous Glycerol	40% Hematocrit Blood
Viscosity (mPas)	3.3	5.2
Density (kg/l)	1.0786	1.055

A rotating speed of 2400 rev/min was chosen for all conditions, due to it being the ideal rotating speed for final applications. The outflow of the pump was occluded to achieve the flow rates required for each condition. Condition 3 represented the ideal operating speed and flow for final applications. For all conditions the inlet was pointing downwards (positive z direction) as shown in figure 6. This particular orientation of the pump represented the least stable in terms of hydrodynamic stability.

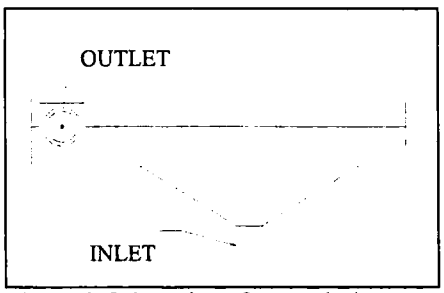

Figure 6. Orientation of pump during measurements

All sensors were calibrated individually for transformation of the output voltage into displacement (μm) values. Calibration involved the use of a computer numerical control (CNC) machine (Benchman XT – Light Machine Corporation 1998) and measurements were acquired through LabView at a sampling frequency of 100 kHz. Also, since the geometry of the four blades of the impeller were not exactly identical to each other, calibration polynomials for each individual blade were also determined.

4. Results and Discussion

Calibration polynomials were determined through the least squares method using Matlab. Orders of polynomials were determined by residual plots as well as calculation of variances. Calibration polynomials for each of the six sensors at each one of the four blades of the impeller were found, resulting in twenty four polynomials.

Output voltages from the sensors for each operating condition were collected through LabView. Samples for 50 impeller revolutions were obtained at a sampling frequency of 50 kHz distributed between the six sensors for all measurements. The corresponding displacement values, in μm, were determined using the calibration polynomials. These values were in turn transformed into displacements in five independent physical coordinates as follows: -

$$x = L2 \tag{1}$$

$$y = L1 \tag{2}$$

$$z = \frac{ECS1 + ECS3}{2} \tag{3}$$

$$\theta x = \tan^{-1}\left(\frac{ECS4 - ECS2}{30000}\right) \tag{4}$$

$$\theta y = \tan^{-1}\left(\frac{ECS3 - ECS1}{30000}\right) \tag{5}$$

Where L1 and L2 were the displacement measurements (in μm) for laser proximity sensors 1 and 2 respectively. ECS 1, ECS 2, ECS 3 and ECS 4 corresponded to the displacement measurements (in μm) for eddy current proximity sensors 1, 2, 3 and 4 respectively. 30000 represented the distance between opposite sensors.

Therefore the average displacement, for 50 revolutions, of the impeller in the five independent physical coordinates about the centre of the bottom surface of the impeller is shown in the following tables. It must be noted that when the impeller was at the origin of the coordinate system, the displacement in the five independent physical coordinates were 0, 0, 115, 0 and 0 for x, y, z, θx and θy respectively.

Table 2
Displacement of impeller in 5 independent physical coordinates for condition 1 (2400 rev/min @ 3 l/min)

Blade Pass	x (μm)	y (μm)	z (μm)	θx (radians)	θy (radians)
1	35.17	88.22	100.22	-0.000015	-0.000217
2	52.27	104.82	101.29	-0.000082	-0.000017
3	40.43	106.75	101.62	-0.000144	0.000139
4	14.64	102.72	102.35	-0.000419	0.000015

Table 3
Displacement of impeller in 5 independent physical coordinates for condition 2 (2400 rev/min @ 4 l/min)

Blade Pass	x (μm)	y (μm)	z (μm)	θx (radians)	θy (radians)
1	25.34	84.13	101.95	0.000089	-0.000400
2	59.34	93.81	106.04	0.000028	-0.000311
3	32.36	98.91	103.82	-0.000031	-0.000095
4	13.58	94.47	105.40	-0.000302	-0.000215

Table 4
Displacement of impeller in 5 independent physical coordinates for condition 3 (2400 rev/min @ 5 l/min)

Blade Pass	x (μm)	y (μm)	z (μm)	θx (radians)	θy (radians)
1	19.42	77.92	102.83	0.000319	-0.000514
2	55.89	83.40	106.91	0.000250	-0.000385
3	24.40	90.05	105.50	0.000172	-0.000249
4	9.86	86.25	107.40	-0.000115	-0.000381

Table 5
Displacement of impeller in 5 independent physical coordinates for condition 4 (2400 rev/min @ 6 l/min)

Blade Pass	x (μm)	y (μm)	z (μm)	θx (radians)	θy (radians)
1	17.28	73.81	103.31	0.000520	-0.000537
2	55.67	77.91	107.05	0.000461	-0.000398
3	23.61	84.12	106.43	0.000338	-0.000286
4	7.86	80.96	108.12	0.000084	-0.000410

From the displacement tables above, the minimum axial displacement was 100.22 μm. By using the following equation, the angular rotation (θ) required for the impeller to touch the pump cavity at this axial displacements was found.

$$\theta = \pm \left[\tan^{-1} \left(\frac{2 \text{ x Displacement}}{30000} \right) \right] \tag{6}$$

Where θ at the minimum axial displacement equals ± 0.0067 radians. This θ value represented the maximum angular displacement allowed before the impeller touches the pump. It can be clearly seen from tables 1 to 4 that the angular displacements in both the x and y directions are lower then the calculated angular displacement, suggesting that the impeller is not touching the pump cavity through angular displacement. Also, since the maximum axial and radial clearances between the impeller and the pump cavity were 230 μm, it can be seen from the tabulated results that the impeller was hydrodynamically suspended within the pump cavity. The maximum and minimum average radial movements in the x and y directions at each blade pass for 50 revolutions at each flow rate are shown in figure 7.

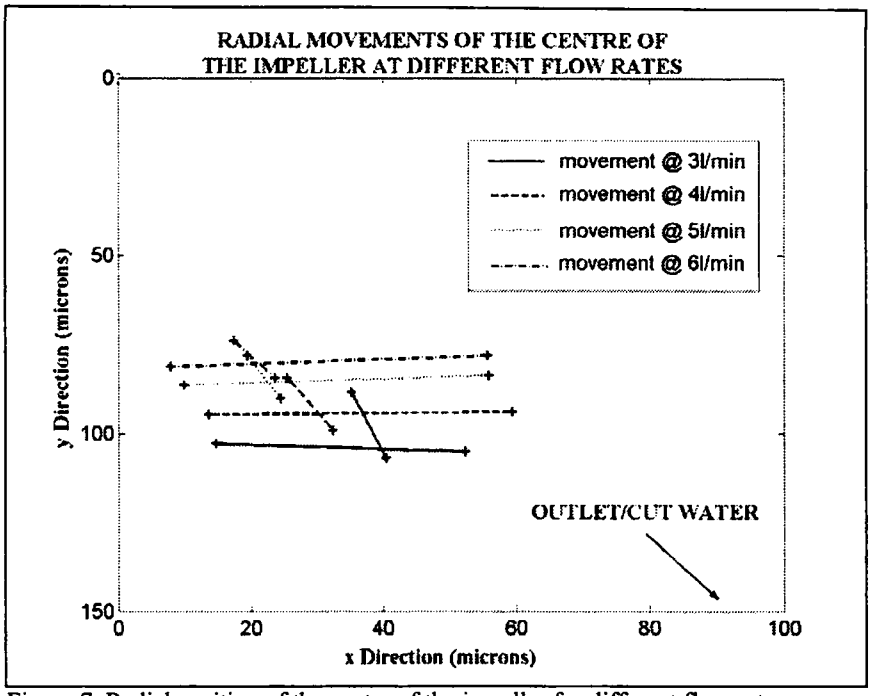

Figure 7. Radial position of the centre of the impeller for different flow rates.

The outlet and cutwater of the pump were positioned at the positive x and y direction. From figure 7, the range in the x direction increased as the flow also increased. The increase in range represented the decrease in stability of the impeller. This behaviour continued until the maximum hydraulic efficiency point of the pump was reached and the impeller was least stable. Previous investigations have found that the maximum hydraulic efficiency occurred at a flow rate of 7 l/min. At this flow rate, the impeller experienced a minimum resultant radial force due to pressure forces around the volute of the pump being constant. Once the flow rate was changed, the pressure forces became inconsistent around the volute, resulting in an increased resultant force and a more stable impeller. This can be described by the stability parameter [12].

Also, figure 7 shows the impeller moving towards the outlet/cutwater of the pump as the flow was decreasing which is also evident in figure 9. This is due to the velocity of the fluid decreasing as it diffused into the outlet, causing the pressure to increase as the velocity decreased. Thus, a low pressure force was experienced after the cut water and a high pressure force at the opposite side of the volute, resulting in a resultant radial force towards the cut water. This phenomenon is typical for centrifugal type pumps (Stepanoff) [13].

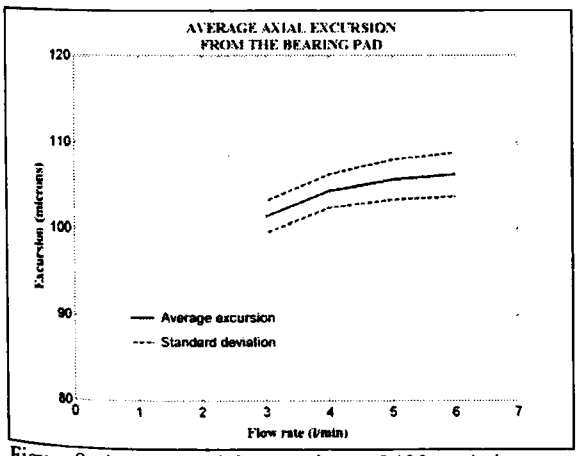

Figure 8. Average axial excursion at 2400 rev/min

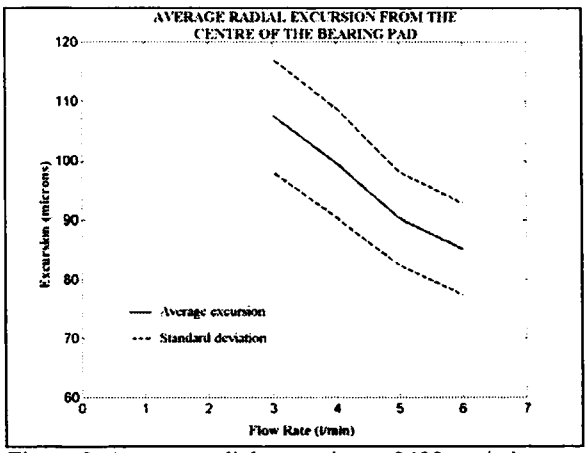

Figure 9. Average radial excursion at 2400 rev/min

Figure 8 represents the axial excursion of the impeller. It can be seen that there was almost no change in the axial excursion for increasing flow rates. This coincides with basic 2-dimensional hydrodynamic theory, which describes the hydrodynamic bearing force, where the bearing force is not a function of the flow rate of the fluid. However, the small changes in excursion that were present, may be due to the inaccuracies in the manual commutation of the rotational speed of the impeller from the motor controller.

5. Further Investigation of Bearing Force

A computer program [14] was developed to calculate the axial bearing force under the bottom surface of an impeller blade. The program solved the Reynolds equation, equation 7, in cylindrical coordinates using finite difference scheme and successive-over-relaxation technique. The calculations assume a constant viscosity and laminar flow, which are both good approximations for this application.

$$\frac{\partial}{\partial r}\left(\frac{\rho r h^3}{\mu}\frac{\partial p}{\partial r}\right)+\frac{\partial}{\partial \theta}\left(\frac{\rho h^3}{\mu r}\frac{\partial p}{\partial \theta}\right)=6\rho(\omega r)\frac{\partial h}{\partial \theta}+12\rho r\frac{\partial h}{\partial t} \tag{7}$$

The total forces on an impeller blade were calculated by adding the forces on each bearing surface and assuming that the top bearings are equivalent to the bottom bearings of equivalent surface area.

The main parameters required by the program include the inside and outside diameters of the impeller, leading and trailing edge clearances of the blade, tilt angle toward the outside diameter of the blade, viscosity of the fluid, rotational speed and the squeeze film velocity (axial velocity) of the impeller. With these parameters the program will calculate the average pressure and its centre under the blade, the total axial bearing force exerted on the blade and the temperature rise. With the bearing force determined, approximations of the stiffness and damping coefficients at each blade were calculated. The coefficients of each blade were then added to give the total stiffness and damping coefficient values.

The following table gives sample calculated results of the total stiffness and damping coefficients for each flow rate.

Table 6
Stiffness and damping coefficients for each flow rate

Flow Rate (l/min)	Stiffness Coefficient (kN/m)	Damping Coefficient (kN.s/m)
3	23.50	5.12
4	22.97	3.35
5	22.28	3.30
6	21.10	2.11

From the calculated results it can be seen that as the flow rate increases, there are only minor changes in the values of the stiffness and damping coefficients. Thus, it can be assumed that the hydrodynamic bearing is stable for all flow rates.

This program is only a preliminary approach for determining an approximation of the axial bearing force exerted on the impeller. Further investigation through experimental work and CFD analysis will be required to obtain more confident results.

6. Conclusions

The determination of the impeller's displacement within the pump cavity was undertaken experimentally. Eddy current proximity sensors and laser proximity sensors were used for the detection of the impeller within the acrylic pump housing. The pump was operated at different flow rates with the impeller rotating at a speed of 2400 rev/min for all conditions.

Results show that under the operating conditions investigated, the impeller was hydrodynamically suspended within the pump cavity. Maximum and minimum average radial movement of the impeller for each flow rate at a constant impeller speed of 2400 rev/min were shown. Results were in accordance to centrifugal pump design. Furthermore, the radial and axial excursion of the impeller was also investigated for each flow rate. Again, results were in accordance with pump design.

Estimations of the stiffness and damping coefficients for the hydrodynamic bearing, for each flow rate, were calculated using a computer program and results from the experiment. Results suggest a stable hydrodynamic bearing for changing flow rates. However, further analysis through experiments and computational fluid dynamics will be needed for obtaining more confident results.

Overall, the method used to perform the experiment discussed in this paper was successful and will also be used for further investigation into the displacement of the impeller within the pump cavity of a current model titanium pump housing. Displacement of the impeller in the five independent physical coordinates were determined and found to be acceptable.

6. References

[1] Kung RT & Hart RM. (1997) Design considerations for bearingless rotary pumps. *Artificial Organs*, **21**(7), 645-650.

[2] Malanoski SB, Belawski H, Horvath D, Smith WA & Golding LR. (1998) Stable blood lubricated hydrodynamic journal bearing with magnetic loading. *ASAIO Journal*, **44**(5), M737-M740.

[3] Wampler R, Lancisi D, Indravudh V, Gauthier R & Fine R. (1999) A sealless centrifugal blood pump with passive magnetic and hydrodynamic bearings. *Artificial Organs*, **23**(8), 780-784.

[4] Mosuzawa T, Kita T, Matsuda K & Okada Y. (2000) Magnetically Suspended Rotary Blood pump with radial type combined motor-bearing. *Artificial Organs*, **24**(6), 468-474.

[5] Allaire P, Hilton E, Baloh M, Maslen E, Bearnson G, Noh D, Khanwilkar P & Olsen D. (1998) Performance of a continuous flow ventricular assist device: Magnetic bearing design, construction, and testing. *Artificial Organs*, **22**(6), 475-480.

[6] Akamatsu T, Nakazeki T & Itoh H. (1992) Centrifugal blood pump with a magnetically suspended impeller. *Artificial Organs*, **16**(3), 305-308.

[7] Hart RM, Filipenco VG & Kung RTV. (1996) A magnetically suspended and hydrostatically stabilized centrifugal blood pump. *Artificial Organs*, **20**(6), 591-596.

[8] Masuzawa T, Kita T, Matsuda K & Okada Y. (2000) Magnetically suspended rotary blood pump with radial type combined motor-bearing. *Artificial Organs*, **24**(6), 468-474.

[9] Watterson PA, Woodard JC, Ramsden VS & Reizes JA. (2000) VentrAssist hydrodynamically suspended, open centrifugal blood pump. *Artificial Organs*, **24**(6), 475-477.

[10] Cook M & Tansley GD. (2000) The dynamic load envelope of the VentrAssist rotary blood pump. In M Umeza, M Arita & N James. (Eds) *Proceedings of the Second Japan-Australia Cardiovascular Bioengineering Symposium*, Sydney, pp.8-9

[11] Massey BS. (1989) Mechanics of fluids - 6th Ed. London: Chapman & Hall Publications.

[12] Akkök M & Ettles CM. (1983) The onset of whirl instability in journal bearings of various bore shapes and groove sizes. *Transactions of the ASME*, **105**(7), 342-352

[13] Japikse D, Marscher WD & Furst RB. (1997) Centrifugal pump design and performance. Vermont, U.S.A.: Concepts ETI, Inc. Publications.

[14] Hogg MC. (2002) Non-linear transient stability analysis of the VentrAssist hydrodynamically suspended impeller. The University of New South Wales, M Biomed Eng Thesis

Acknowledgements

Financial support for this research is provided jointly by the Australian Research Council (Grant No. C8992011), the University of Technology, Sydney and VentrAssist Pty. Ltd. Australia.